Neutron and x-ray scattering study of phonon dispersion and diffuse scattering in (Na,Bi)TiO_{3}-xBaTiO_{3} single crystals near the morphotropic phase boundary

Chengtao Luo, Dipanshu Bansal, Jiefang Li, Dwight Viehland, Barry Winn, Yang Ren, Xiaobing Li, Haosu Luo, and Olivier Delaire

Phys. Rev. B **96**, 174108 — Published 10 November 2017
DOI: 10.1103/PhysRevB.96.174108

Neutron and x-ray scattering study of phonon dispersions and diffuse scattering in (Na,Bi)TiO3-xBaTiO3 single crystals near the morphotropic phase boundary

Chengtao Luo [a)]

Materials Science and Engineering, Virginia Tech, Blacksburg, Virginia 24061, USA

Dipanshu Bansal

Materials Science & Technology Division, Oak Ridge National Laboratory, Oak Ridge, TN 37831, USA

Jiefang Li, Dwight Viehland

Materials Science and Engineering, Virginia Tech, Blacksburg, Virginia 24061, USA

Barry Winn

Quantum Condensed Matter Division, Oak Ridge National Laboratory, Oak Ridge, TN 37831, USA

Yang Ren

X-ray Science Division, Argonne National Laboratory, Argonne, IL, 60439, USA

Xiaobing Li, Haosu Luo

Shanghai Institute of Ceramics, Chinese Academy of Sciences, 215 Chengbei Road, Jiading, Shanghai 201800, China

Olivier Delaire [b)]

Mechanical Engineering and Materials Science Department, Duke University, Durham, NC 27708 and Materials Science & Technology Division, Oak Ridge National Laboratory, Oak Ridge, TN 37831, USA

a) Electronic mail: lchentao@vt.edu b) Electronic mail: olivier.delaire@duke.edu

Abstract

Neutron and x-ray scattering measurements were performed on $(Na_{1/2}Bi_{1/2})TiO_3$-xat%$BaTiO_3$ (NBT-xBT) single crystals (x = 4, 5, 6.5, 7.5) across the morphotropic phase boundary (MPB), as a function of both composition and temperature, and probing both structural and dynamical aspects. In addition to the known diffuse scattering pattern near the Γ-points, our measurements revealed new, faint superlattice peaks, as well as an extensive diffuse scattering network, revealing a short-range ordering of polar nanoregions (PNR) with a static stacking morphology. In samples with compositions closest to the MPB, our inelastic neutron scattering investigations of the phonon dynamics showed two unusual features in the acoustic phonon branches, between the super-lattice points, and between the super-lattice points and Γ-points, respectively. These critical elements are not present in the other compositions away from the MPB, which suggests that these features may be related to the tilt modes coupling behavior near the MPB.

1. Introduction

It has been nearly 50 years since the first atomic-level ferroelectric microscopic theory was published by Cochran and Anderson [1], which was based on their study of lattice dynamics. The concept of soft-modes in the phonon dispersions was introduced to describe the slowing of vibrational frequency, all the way to freezing, for transverse optical phonon modes (TO) during ferroelectric transformations. The TO mode condensation results in static ionic displacements below the transition temperature, thereby producing large permanent spontaneous polarizations and crystal lattice distortions. The soft-mode concept describes the common characteristics many proper and improper ferroelectric transformations, most known polar transformations, including anti-ferroelectric ones, although some are thought to arise from a change in magnetic order or electronic/orbital structure. The soft-mode theory has been experimentally validated by inelastic neutron scattering (INS) and Raman spectroscopy measurements in a number of compounds, most notably in conventional ferroelectric systems such as $PbTiO_3$ [2, 3]. The physical picture of the ferroelectric transition in disordered, so-called relaxor systems, remains less clear, however. X-ray diffuse scattering and INS are powerful experimental techniques for investigating the specific microstructure and mechanisms underpinning piezoelectric behavior through phonon analysis. Here, we apply these experimental techniques to the study of NBT-xBT.

Based on the unique characteristics of “relaxor” ferroelectrics—and in particular the ultrahigh piezoelectric properties of $Pb(Mg_{1/3}Nb_{2/3})O_3$-$PbTiO_3$ (PMN-PT) and $Pb(Zn_{1/3}Nb_{2/3})O_3$-$PbTiO_3$ (PZN-PT)—significant efforts have been directed at extending the soft-mode theory in order to account for their unusually slow dynamical transition and relaxation mechanism [4-7]. Relaxor systems have also been developed in Pb-free perovskite solid solutions, which exhibit many of the properties of Pb-based systems [8]. Following the strategy of adding $PbTiO_3$ (PT) to PMN to produce remarkably high piezoelectric response in the PMN-PT solid solution, $(Na_{1/2}Bi_{1/2})TiO_3$ (NBT) alloyed with $BaTiO_3$ (BT) was also found to form an analogous solid solution between relaxor and normal ferroelectrics, with a morphotropic phase boundary (MPB) between rhombohedral (R) and tetragonal (T) phases [8]. Consequently, $(Na_{1/2}Bi_{1/2})TiO_3$–xat%$BaTiO_3$ (NBT-xBT) and $(Na_{1/2}Bi_{1/2})TiO_3$–xat%($K_{1/2}Bi_{1/2})TiO_3$ (NBT-xKBT) ceramics and single crystals have been developed and studied [9, 10].

In addition to two different kinds of intrinsic ferroelectric polarization, NBT-xBT also features two improper ferroelectric oxygen octahedral tilt systems in R and T phases, which can be identified by characteristic super-lattice structures (P4bm/R3c), as shown in Figure 1a. In the Glazer notation, these octahedral tilt systems are designated as in-phase $a^0a^0c^+$ and anti-phase $a^-a^-a^-$ [11]. These different tilt systems result in distinct super-lattice Bragg reflections in reciprocal space, which are readily identified in diffraction experiments. The in-phase tilt belongs to T-phase (P4bm) and has super-lattice peaks at the M-point, while the anti-phase one belongs to R-phase

(R3c) and has super-lattice peaks at the R-point. M- and R-points have crystallographic indices of the form ½(ooe) and ½(ooo), respectively (o for odd and e for even). The locations of both the M- and R-points in reciprocal space are illustrated in Figure 1b in the case of a pseudocubic lattice [12]. These rotational modes are the result of acoustic phonon modes that condense at the Brillouin zone boundaries. Although these are typically non-polar modes, they have been reported to couple with polarization through rotostriction [13]. To explain the phase coexistence and the relaxor behavior, a model of polar nanoregions (PNRs) similar to that developed for Pb-based relaxors was also introduced [4, 14]. In details, the coexistence of M-point derived (P4bm) PNRs and R-point derived (R3c) PNRs has already be used to explain electron diffraction result [10, 14]. Yao et.al. reported the volume fraction of the M-point derived (P4bm) PNR increases with increasing x as the MPB is approached [14]. The PNR concept is a popular model to link the extraordinary properties of Pb-based ferroelectric relaxors [15-18] to the microstructure. Presently, one of the main problems in applying PNR-based models in NBT-xBT system is that the coupling of the two oxygen tilt systems is still unclear and requires further investigations.

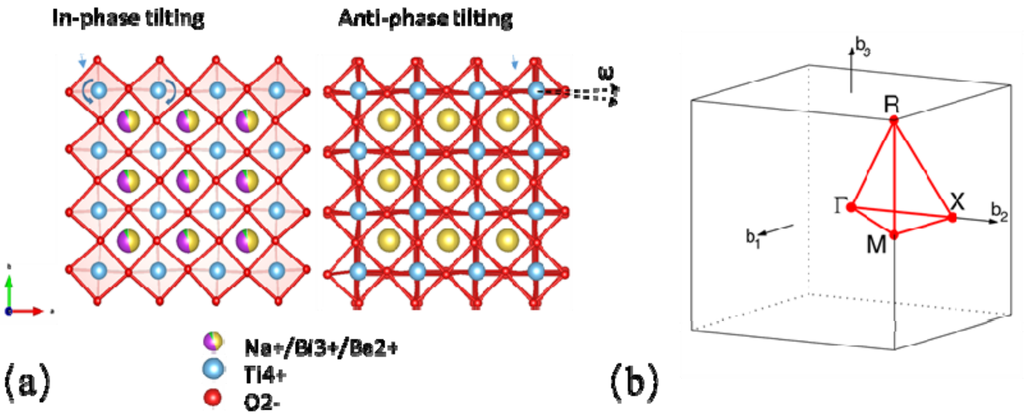

Figure 1: Background figures: (a) NBT-BT super-lattice structure comparison (P4bm for NBT-7BT and R3c for NBT); (b) high-symmetry points notation in reciprocal space for pseudocubic NBT-BT.

The analysis of the atomic displacements in these tilt systems can be performed via X-ray diffraction (XRD) [19, 20], electron microscopy [21, 22], or neutron scattering techniques [4, 23], which enable one to track the phase transition and domain structures. Neutron scattering in particular has been widely used to study different types of relaxors including the Pb-free ones [4, 23-25]. For NBT-xBT solid solutions, different geometric patterns in the diffuse (elastic) scattering were previously investigated to characterize the different phases [23]. Further, INS studies were performed on the undoped system NBT [26, 27]. Here, we extend these prior studies and investigate trends in mode softening, super-lattice points, and diffuse scattering in more detail in the NBT-xBT system, in order to probe the dynamic mechanism underlying piezoelectric/relaxor behavior. Extensive characterization near the MPB of the NBT-xBT system was performed by means of synchrotron single-crystal XRD and INS experiments. In addition to the known diffuse scattering patterns near the Γ-points, a super-lattice point and a diffuse scattering network was observed, revealing a short-range ordering in the PNR static stacking morphology. In our studies of atomic dynamics with INS, two acoustic-like modes are identified, with a possible connection to the diffuse signal seen in XRD. One is between the super-lattice points, and the other is between the super-lattice points and Γ-points. These features are not seen in compositions away from the MPB, which may shed light on specific dynamics near the MPB that impact the high piezoelectric response.

2. Experiment

High-quality single-crystals of NBT-xBT (x=4, 5, 6.5,7.5%) were grown by a top-seeded solution growth method. The compositions of the solid solutions in the as-grown condition were determined by inductively coupled plasma atomic emission spectrometry (ICPAES).

Neutron scattering measurements were performed using the hybrid spectrometer (HYSPEC [28, 29], BL-14B) at the spallation neutron source (SNS) at Oak Ridge National Lab (ORNL). Using HYSPEC, the dynamical structure factor S(Q, E) was mapped for crystals of NBT-5BT (mass: 1.984g) and NBT-6.5BT (0.882g) at room temperature and 600K. Additional compositions NBT-4BT (11.457g)/NBT-5BT (39.009g)/NBT-7.5BT (14.814g) were measured at 300K/540K/700K.

High-energy XRD measurements were performed on beam line 11-ID-C (λ=0.11725Å and E=105.8 keV) at the Advanced Photon Source (APS) at Argonne National Laboratory (ANL). The 2D-images were collected in the forward direction using a Perkin-Elmer large area detector. The diffraction patterns were analyzed using the FIT2D software. The distance from sample to detector and instrumental parameters were determined by refining the profiles from standard CeO_2 samples.

3. Results

In this study, all the reciprocal space results were indexed under a pseudocubic lattice. The first neutron dataset is based on the (HK0) planes to focus on the M-points while the second neutron dataset is based on the (HHL) planes to focus on the R-points. The energy integration range of all the elastic mappings is from -1 meV to 1 meV. The energy ranges of INS results are 0 meV to 13 meV for first dataset, and 0 meV to 20 meV for second one. Both INS datasets were supplemented by corresponding XRD results.

All the INS results use the symmetry labels convention of Cowley et al. (Appendix I of [30]) to refer to the different normal modes. All the color maps represent the neutron scattering intensity plotted on a logarithmic scale, which is unformed in each sample.

The temperature points selected in this work are based on the characteristic temperatures of NBT-5.6BT [31]. In particular, the depolarization temperature T_d is 403K, dielectric maximum temperature (Curie temperature) T_m is 560K, and Burns temperature T_B is near 650K.

3.1. Elastic neutron scattering in (HK0) plane

The elastic neutron scattering patterns in Figure 2a-c focused on the (HK0) planes of NBT-5BT at 300K (a), NBT-6.5BT at 300K (b), and NBT-5BT at 600K (c). The slices were centered on the (200) zone and contained multiple M-points. Due to the fact that the ½(3±10) points overlapped with an Al powder diffraction ring from the sample holder, the M-point data discussed later will only consider the ½(5±10) reflections.

In general, changes in temperature and composition did not appear to significantly impact the resulting elastic neutron scattering patterns shown for these slices. Similar diffuse scattering near (200) and (210) were already observed in prior XRD [31] and neutron [23] studies. In both compositions investigated herein, the scans showed oval-shaped scattering patterns around (210) with a <110> orientation and half-X-shaped scattering around (200), as showin in right panels in Figure 2b. These features are characteristic of the tetragonal side of the MPB [4, 23]. Generally, the diffuse scattering for NBT-5BT was more intense than in NBT-6.5BT. Note that NBT-5BT is closer to the MPB, and features enhanced piezoelectric properties.

In-phase oxygen octahedral tilting super-lattice reflections at M-points, were evident in all slices. These M-points were surrounded by isotropic diffuse scattering intensity in the (HK0) plane. In the top-right panel of Figure 2b, one can note the presence of diffuse scattering intensity connecting the (120) and (210) zones, which crosses the forbidden point ½(330), as shown by the dashed white line with arrows and red cross. Here, the dashed white line with arrows is parallel to the actual diffuse scattering and used only to indicate the directions. This type of diffuse scattering connection was not observed toward the M-point ½(510), as will be further discussed with respect to INS studies.

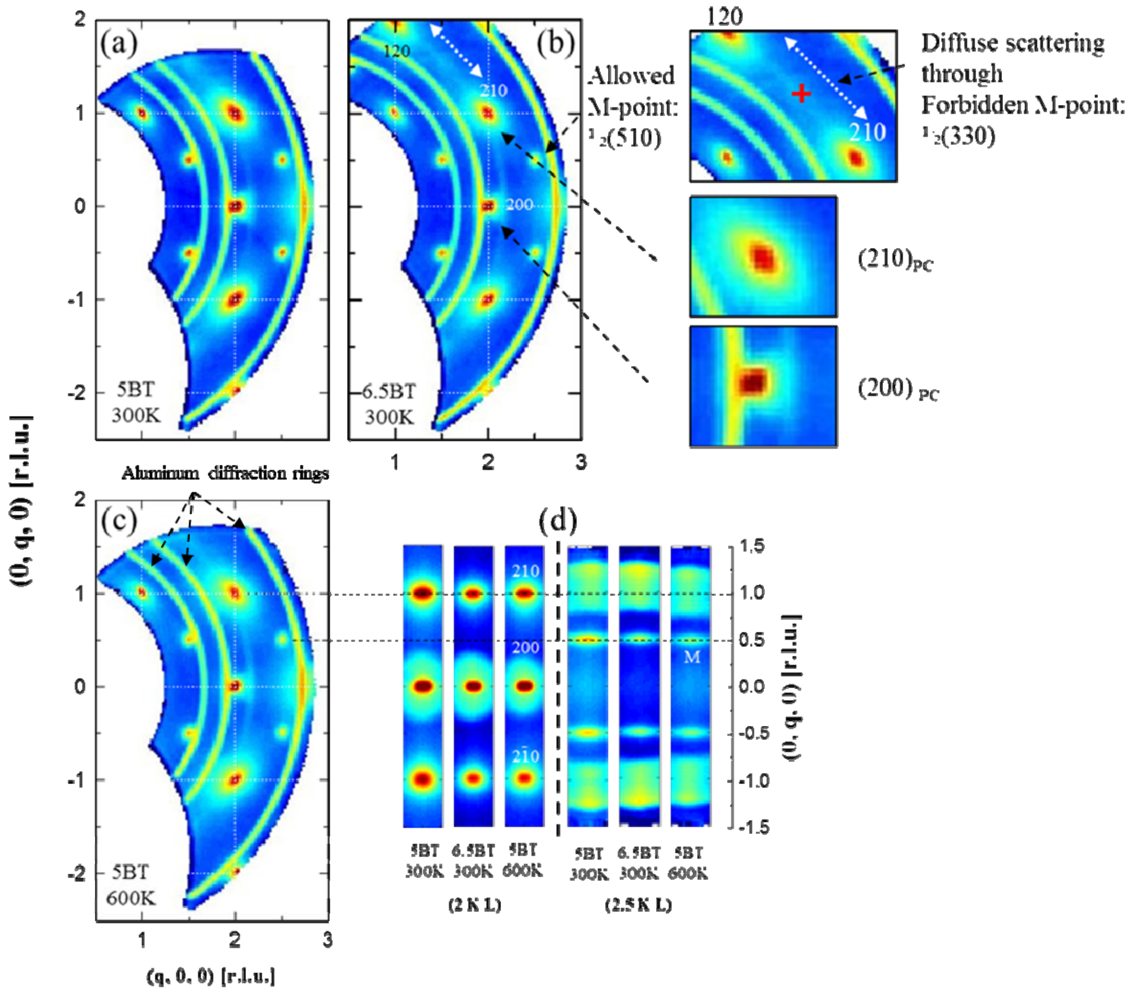

Figure 2: Elastic neutron scattering patterns of (a) NBT-5BT at 300K, (b) NBT-6.5BT at 300K, (c) NBT-5BT at 600K in the (HK0) plane and (d) (2KL)/(2.5KL) plane. The horizontal and vertical axes are along [H00] and [0K0] directions respectively in the (HK0) plane, and [00L] and [0K0] directions for the (2KL) and (2.5KL) plane, respectively.

We observed both symmetry-allowed (½(510), ½(310)) and symmetry-forbidden (½(330)) super-lattice reflections in the tetragonal phase of NBT-xBT with the P4bm space group symmetry. The forbidden M-point ½(hhl)/(-hhl) is due to the unique oxygen octahedron connection (see Figure 1a). In the (HK0) plane and for the case of P4bm, neighboring oxygen octahedra have opposite tilting directions, which generates the super-lattice structure $a^0a^0c^+$; this finding also indicates that the oxygen octahedra along [HH0]/[-HH0] direction share a common tilting direction. Therefore, the related super-lattice points at ½(hh0)/(-hh0) are forbidden. And for single crystals, the further ½(hhl)/(-hhl) are also forbidden. Although this feature is not common in selected area electron diffraction (SAED) [32, 33], it has been observed in results generated by high-energy XRD and software simulation based on the P4bm symmetry [34, 35]. In further discussions, we refer to the two types of M-points as "allowed" and "forbidden". Both types of M-points are shown in Figure 2b. The forbidden ½(330) is marked by a red cross.

In order to further compare the elastic scattering between the Bragg peaks and the M-points, additional slices (Figure 2d) along different directions were extracted from the same S(Q, E) dataset. The slices on the left part of Figure 2d illustrate the (2KL) planes covering the Bragg peak (200)/(2±10), and those on the right side show the (2.5KL) plane covering the M-point ½(5 ±1 0). Note that the data in Figure 2d shares the vertical [0K0] axes with Figure 2c, where dashed lines are drawn to help align the same Bragg peaks and M-points. On the horizontal [00L] axes of Figure 2d, the Q-range covers a range of -0.2 and 0.2 reciprocal lattice units (r.l.u.). The scattering patterns in the planes (2KL) and (2.5KL) are clearly different from each other. The scattering near the Bragg peaks is isotropic, whereas the scattering near the M-points shows a spindle-shaped feature along the [001] direction.

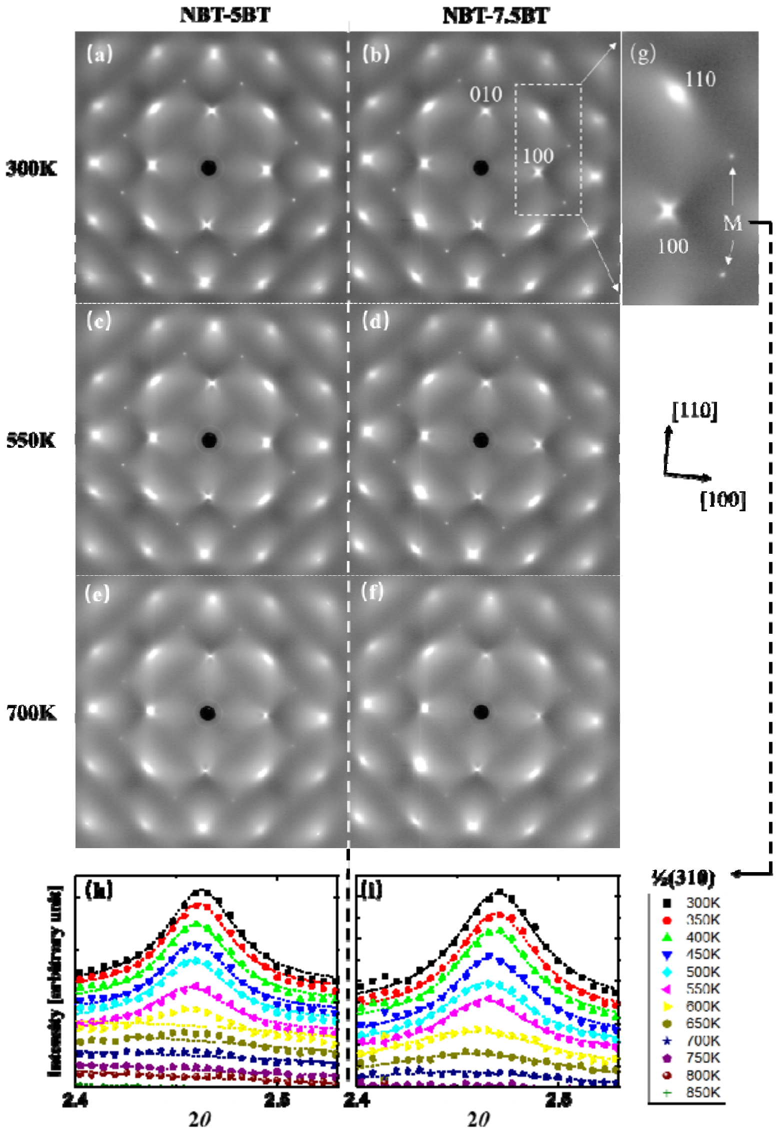

Figure 3: XRD scattering patterns along the (HK0) planes from (a)(c)(e) NBT-5BT, and (b)(d)(f) NBT-7.5BT at (a)(b) 300K, (c)(d) 550K and (e)(f) 700K. One area in (b) is enlarged in (g) to provide higher resolution pictures of the diffuse scattering features and M-points ½(3±10). Integration of the intensity for ½(310) peak was made over a broad temperature range, as summarized in (h) NBT-5BT and (i) NBT-7.5BT. Fixed offsets were used between two neighboring curves to make comparisons easier.

We now discuss the single-crystal XRD data measured with the APS beamline 11-ID-C. Figure 3a-f illustrates the diffuse scattering pattern observed in the (HK0) reciprocal plane. These data reveal diffuse ridges along the <110> directions, X-shaped patterns around (H00), and super-lattice peaks at M-points as illustrated in the zoomed-in area in Figure 3g. These diffuse scattering patterns thus show similar features as those noted from the neutron investigations provided in Figure 2.

As shown in Figure 3, a clear (110)-oriented diffuse scattering intensity can be seen for both (x=5, 7.5) crystals. Strong X-shaped diffuse scatting features around the (q00)/(0q0) reflections in Figure 3 confirm that the elastic diffuse scattering features in the neutron data taken near (200) were incomplete since they were partly obstructed by aluminum rings. Unlike NBT [23], neither NBT-5BT nor NBT-7.5BT exhibit sharp changes in their diffuse scattering patterns with increasing temperature. Although XRD measurements were performed over a temperature range from 300K to 950K, Figure 3a-f only shows three temperatures: 300K, 550K (near the dielectric constant maximum), and 700K.

The evolution with temperature of the intensity of ½(310) M-points is shown in Figures 3h-i. In a uniform integration area around the ½(310), the intensities with same 2θ are integrated and the resulting curves of integrated intensity-vs-2θ are plotted. Curves for different temperatures are offset vertically to facilitate comparison and fitted by Lorentzian functions. The common feature of these two datasets is that there is no peak intensity jumps near the Curie temperature (560K) and depolarization temperature (403K), and such intensity changing pattern will be compared to R-point and discussed below. Furthermore, the FWHMs are not changed in both datasets under the 550K. In details, FWHMs of NBT-5BT have a mean value of 0.0434±0.0047 and a standard deviation of 0.0024, while FWHMs of NBT-7.5BT have a mean value of 0.0503±0.0034 and a standard deviation of 0.0015. Such a temperature-independent FWHM of superlattice point is previously unreported. It indicates that the average size of M-point derived PNRs is also independent of temperature (within the resolution of our experiment). Also, the result indicates that M-point ½(310) peaks are sharper in NBT-5BT than in NBT-7.5BT, showing such superlattice structure has a longer range ordering in NBT-5BT.

3.2. Inelastic neutron scattering in (HK0) plane

The INS data around (200) Bragg peak is shown in Figure 4, divided into two panels. The top row presents the data for transverse Δ_5 phonon modes, which were folded along the [H00] axis. The data folding adds up the signals from (2, -q, 0) to (2, q, 0) to improve the statistical quality of the data for subsequent peak fitting. The folding is based on the pseudocubic symmetry, and is only used for transverse modes (Figure 4a-c). The bottom row presents the data for the longitudinal Δ_1 phonon modes. Superimposed on these maps, the results of fits for the position of the peaks are shown, for fits performed using both constant-Q cuts and constant-E cuts. The constant-Q cut results are shown as black squares with vertical error bars, and results from constant-E cuts are indicated by the white squares with horizontal error bars.

In Figure 4a, the NBT-5BT crystal at 300K exhibits a “waterfall” effect, where the TO phonon drops from 11meV to 7meV (into the TA mode) at the reduced phonon wavevector q~0.17. This feature has been previously reported for both NBT [26] and PMN [36]. At 600K (see Figure 4b), the waterfall effect is less pronounced, which is indicated by the weaker TO phonon and its shifting along q. On the other side, the TA phonons are not obviously influenced by the temperature rising, and the TO mode still softened into the TA mode at the same q, showing the coupling of TA/TO modes is weakly dependent on temperature. In Figure 4c, the TO phonon of NBT-6.5BT can be seen to have a similar “drop” at the same q~0.17; however, the extent of this drop is not as steep as that in Figure 4a. Compared to the different FWHM of NBT-5BT (0.0434) and NBT-6.5BT (0.0503) within Figures 3h-i, the waterfall effect location here is not affected by the different composition, as well as the different sizes of the M-point derived PNR. Note that at 600K, above the Curie temperature, the M-points in the (HK0) plane are still observable, and here the persistence of the waterfall effect at this temperature indicates that the M-point PNR may play an important role in the lattice dynamics through the TO mode.

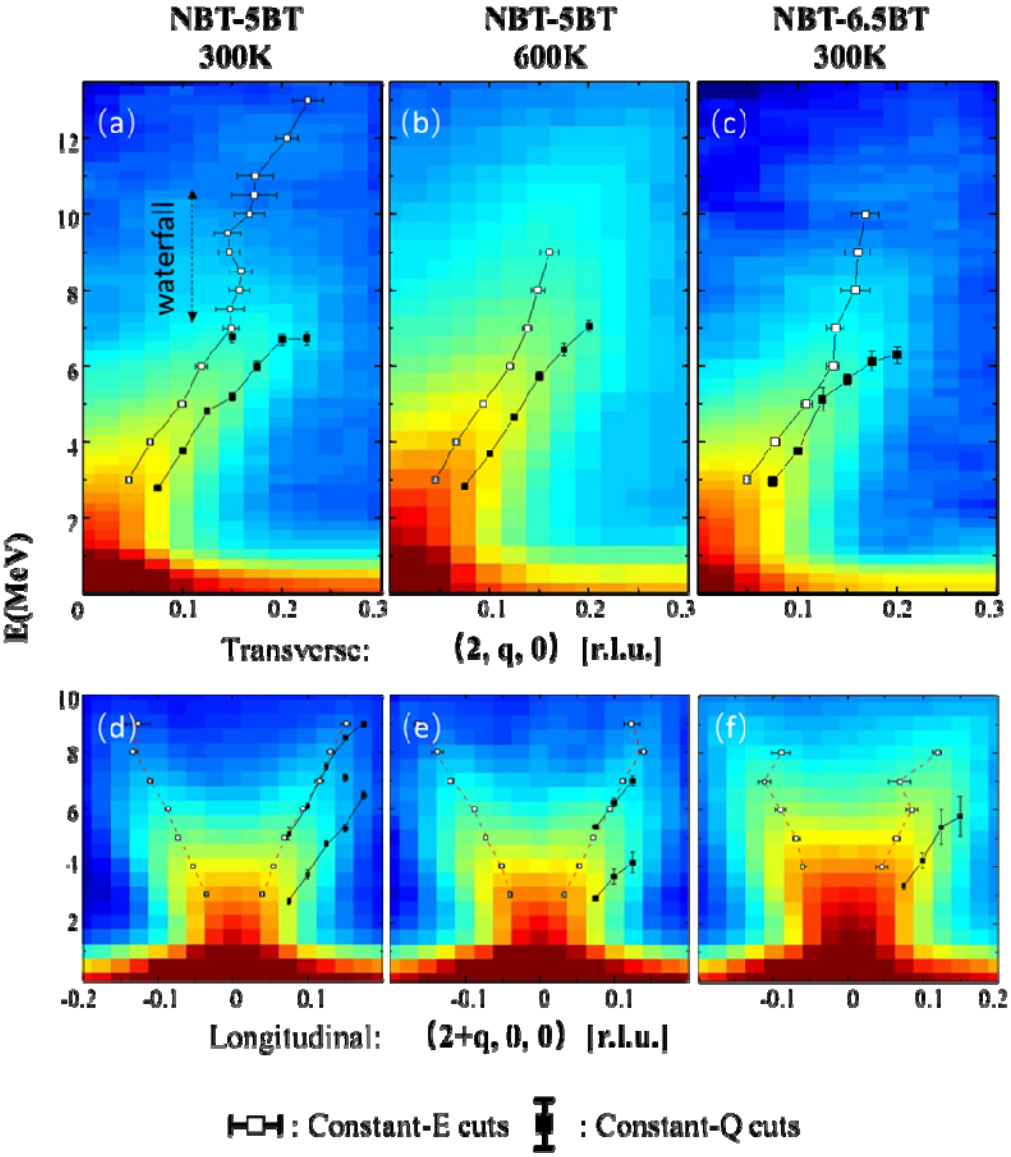

Figure 4: Inelastic neutron scattering taken near the (200) Bragg peak. The figure is divided into three columns for (a)(d) NBT-5BT at 300K, (b)(e) NBT-5BT at 600K and (c)(f) NBT-6.5BT at 300K. Likewise, it is divided into two rows for phonons in (a)(b)(c) transverse modes and (d)(e)(f) longitudinal modes.

For the longitudinal Δ_1 phonon modes, the changes with temperature or composition are limited, as can be seen in Figures 4d-f. Unlike previous studies involving NBT [26], the LO branches in Figures 4d-f are not observed to drop into the LA branches; nor was any LA branch splitting observed. We did, however, observe strong inelastic diffuse scattering near the in-phase super-lattice reflections (M-points), as shown in Figure 5. Striking intense scattering "columns" (intensity signal spread over a broad range of energies at a fixed wave vector) were observed above the allowed M-points up to about 8meV, along the [2.5K0] direction (see Figures 5a-c). These M-point columns showed no distinguishable q-broadening with increasing energy. The intensity and height of these columns were not significantly impacted by changes in temperature or BT content (5%/6.5%).

In addition to the intense columns at M-points, intensity along [110] corresponding to transverse Σ_3 modes near the (210) zone is observed (see Figures 5d-f), connecting to an M-point column. In contrast, previous results in elastic scattering (Figure 2a-c) revealed that the allowed M-points were not connected to any Bragg peaks by diffuse features in the (HK0) planes. These Σ_3 modes in Figures 5d-f illustrate the similar connection to the M-point columns. Considering the compatibility relations between the Σ and M modes [30], the TA Σ_3 mode can only connect to the M_3 modes at the M-points, and such TA Σ_3-M_3 connection is shown by the a dashed line in Figure 5d-f. Thus, the M-point columns can be identified as acoustic M_3 modes, which has the lowest frequency within all M modes and represents the oxygen octahedra in-phase tilting along c-axis only.

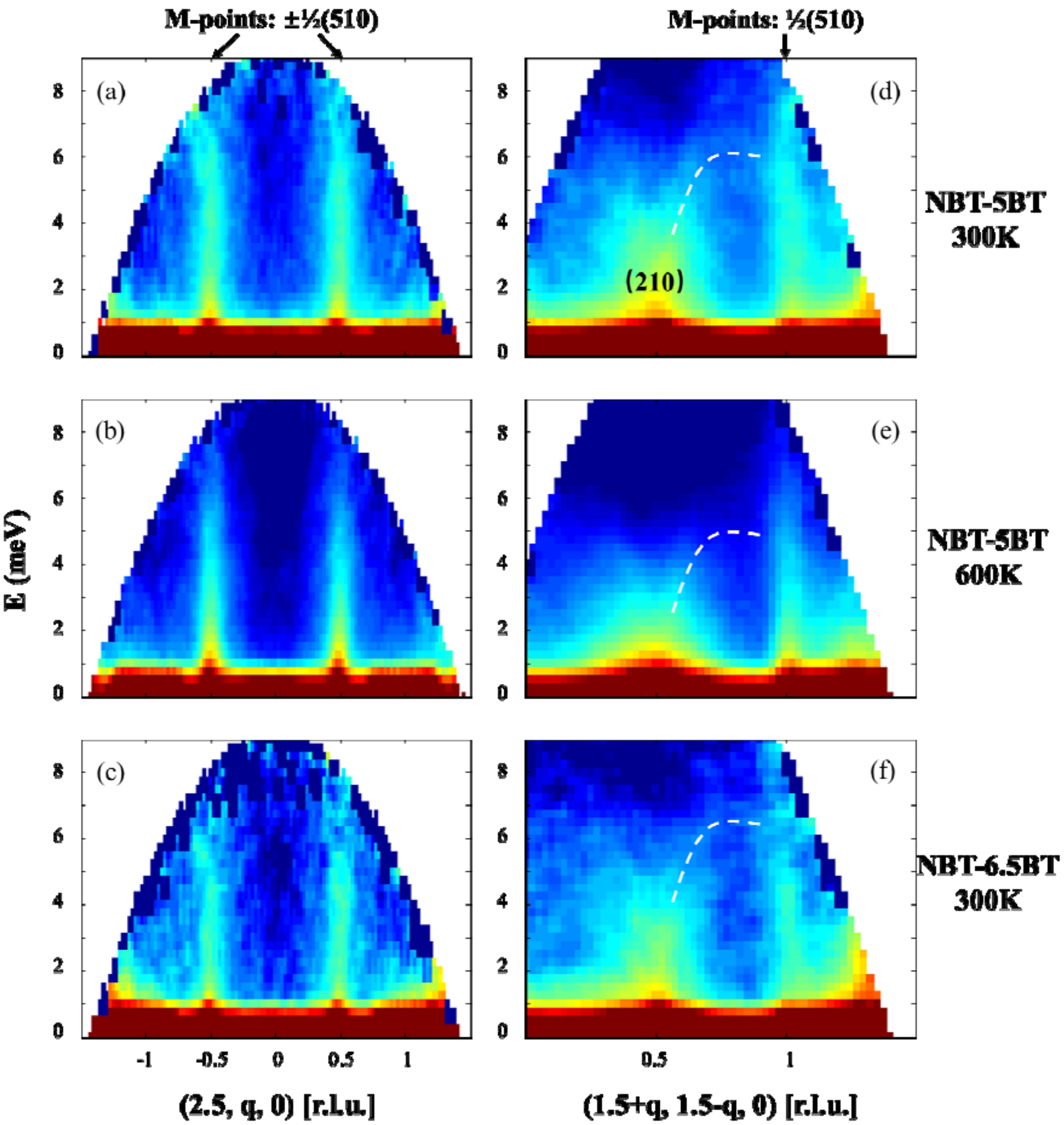

Figure 5: Inelastic neutron scattering of (a)(d) NBT-5BT at 300K, (b)(e) NBT-6.5BT at 300K and (c)(f) NBT-5BT at 600K. These data were taken along the (a)(b)(c) (2.5, q, 0) and (d)(e)(f) (1.5+q, 1.5-q, 0). The energy columns near the allowed M-points ½(5±10) are marked by arrows in (a) and (d).

3.3. Elastic neutron scattering in (HHL) plane

Figures 6a-f show a panel of elastic neutron scattering patterns for NBT-7.5/5/4BT at temperatures of 300/540/700K. These data were taken in the (HHL) plane. The horizontal and vertical axes are along the directions [00L] and [HH0], respectively.

First, multiple arc-shaped features can be seen for both NBT-5BT and NBT-7.5BT, which reflect varying sample mosaic quality. Second, both M-points and R-points can clearly be seen to coexist. Detailed 1-D cuts across different zones are shown in Figures 6h-j. We note again that the M-points ½(330) are forbidden in a perfect P4bm space group, as indicated in reference to Figure 2.

Figures 6h-j focus on the [-1.5, -1.5, q] direction from the 1-D cuts. These cuts cross both the forbidden M-points and the R-points. In each sub-figure, the peaks from left to right are the R-point ½(-3, -3, 1), the forbidden M-point ½(-3, -3, 0) and the R-point ½(-3, -3, -1), as indicated. One should note that the forbidden ½(-3, -3, 0) reflection has a weak, broad and isotropic diffuse scattering shape. This is likely due to imperfections in the larger crystals. Here, the observations for the forbidden M-points are quite different from the sharper and more intense behavior in the (HK0) plane for the allowed M-points. It is worth mentioning that the NBT-5BT crystal featured strong mosaic arcs at room temperature (black line in Figure 6i and red line in Figure 6j) near the R-points, making the analysis of peak intensities (Figures 6h-j) difficult. So, the 1-D cut of NBT-5BT at room temperature will not be discussed. Compared to data shown in Figure 3, the forbidden M-points in Figures 6h-j have similar features with changes in temperature between samples; specifically, the peak intensity decreases gradually with increasing temperature, but maintains the same FWHM.

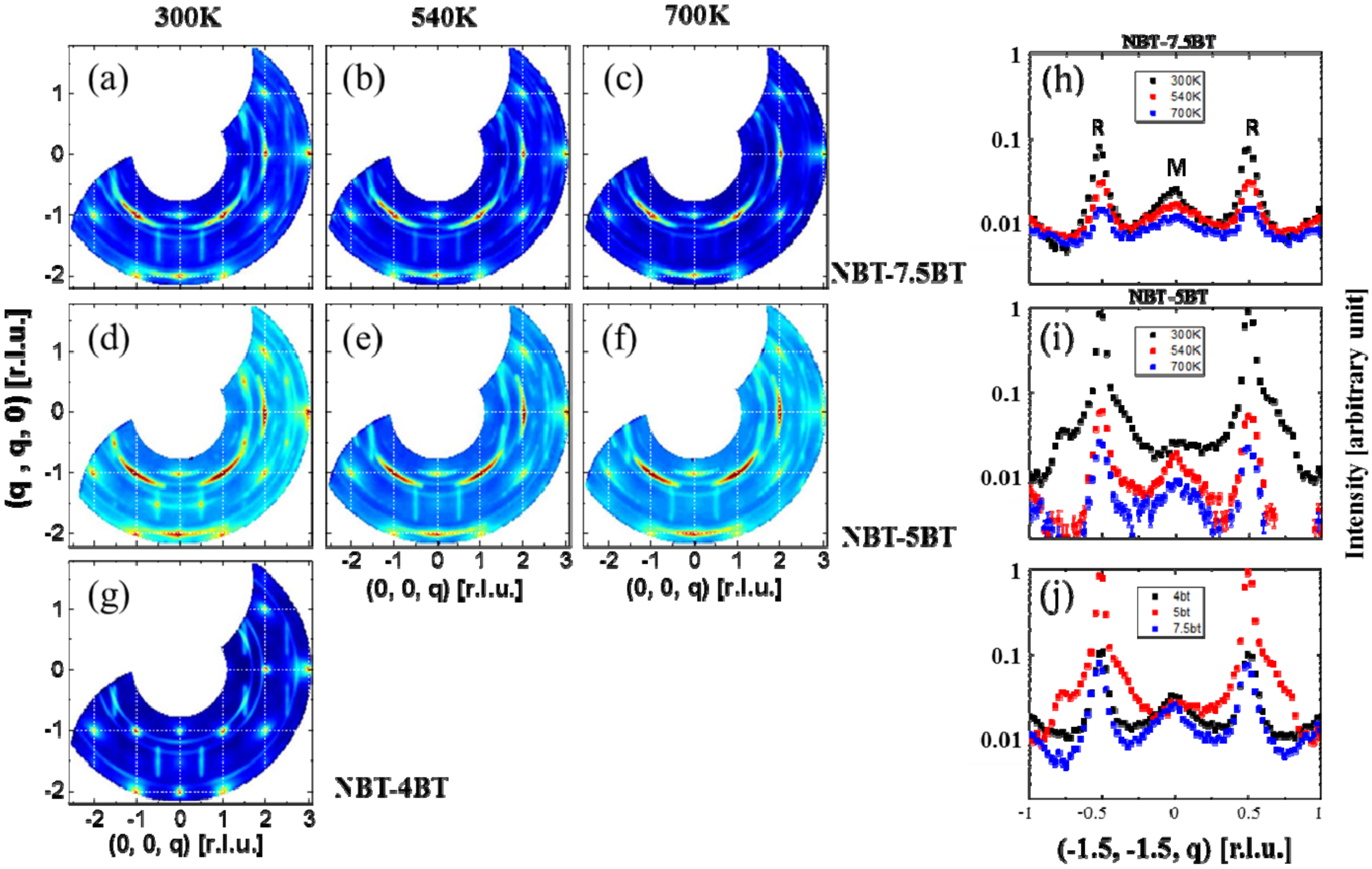

Figure 6: Left panel (a)~(g): Neutron elastic scattering patterns taken in the (HHL) plane for (a)-(c) NBT-7.5BT, (d)-(f) NBT-5BT and (g) NBT-4BT. The horizontal and vertical axes are along [00L] and [HH0], respectively. Right panel (h)-(j): Super-lattice changes for NBT-xBT based in the (HHL) neutron data. Plots compare (h)(i) the same BT contents at different temperatures, and in (j) the various BT contents at room temperature, respectively. The M-point in (h)-(j) are from the forbidden ½(-3, -3, 0) zone.

An additional feature that can be noted in Figure 6 is the unique vertical rod-shaped diffuse scattering around all the observable R-points along the [HH0] direction. Figure 7 proves that such rod-shaped scattering near the R-points arises from the projection of the X-shaped diffuse scattering within the measurement volume.

Figure 7 shows the 3-D neutron elastic scattering patterns taken near the R-point ½(-3, -3, 1). The 3-D plots axes are along the [00L], [HH0] and [-HH0] directions. The rod-shaped diffuse scattering becomes X-shaped in the 3-D view. The diffuse streaks across the R-point are along the [100]/[010] directions (see Figure 7g). The isovalues of contour intensity at 300K are set differently as 0.039 for NBT-7.5BT, 0.080 for NBT-5BT and 0.037 for NBT-4BT. Also, the relative isovalues for 300K/540K/700K of all samples are set as 8/6/5. These settings are decided in order to make the background signals in a similar level and show the 3-D diffuse scattering shapes more clearly. Such X-shaped diffuse scattering near the R-points is part of a much larger network, and here its boundaries are caused by the limited [-HH0] range in S(Q, E) dataset. With changes in temperature, these diffuse scattering streaks followed the R-point in the center, and both were suppressed during heating process. Such intensity change pattern fits to the result from Figure 6h-i.

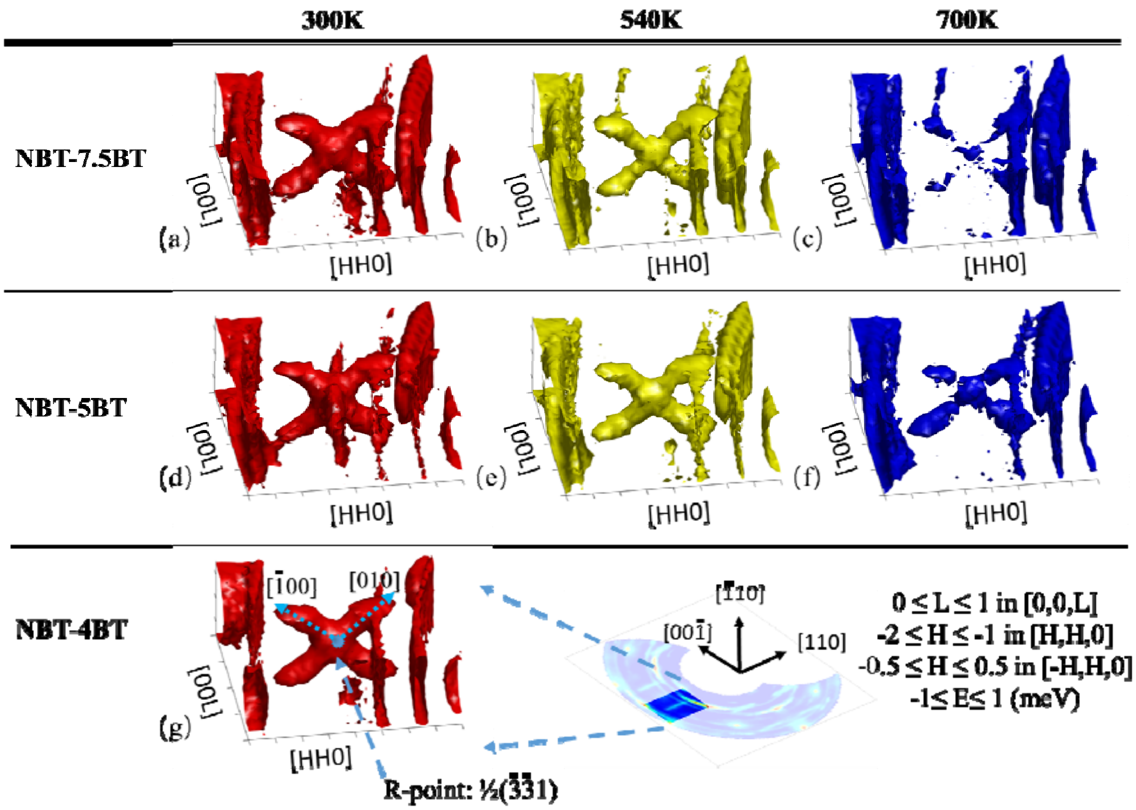

Figure 7: 3-D neutron elastic scattering patterns around the R-point (-3/2, -3/2, 0.5) for (a)-(c) NBT-7.5BT, (d)-(f) NBT-5BT and (g) NBT-4BT. The three axes on each figure are along the [00L], [HH0] and [-HH0] directions. All the plots share the same range of [0, 1] in [00L], [-2, -1] in [HH0] and [-0.5, 0.5] in [-HH0]. Colors mark different temperatures, (a)(d)(g) red at 300K, (b)(e) yellow at 540K, and (f)(h) blue at 700K. Dashed arrows in (g) shows the selected 3-D reciprocal space location based on Figure 6a. The isovalues of contour intensity at 300K are set as (a) 0.039, (d) 0.080, (g) 0.037, and the relative isovalues for 300K/540K/700K are 8/6/5.

These diffuse scattering streaks have two main characteristics. They exhibit [100]/[010] orientations, and they cross at the R-points. They are also observed in XRD measurements for NBT-5BT. Figure 8 shows the XRD scattering patterns obtained at APS for NBT-5BT at different temperatures. The scanning surface is tilted from the (HK0) plane along the [010] axis in order to reach the near R-points ½(511) and ½(531) in the enlarged regions. Smaller images on the right of Figure 8a provide a magnified portion of the area focusing on the allowed M-points at ½(501) and the R-points at ½(511). Note also that Figure 8a clearly shows the existence of the diffuse scattering network along [100]/[010] directions. The streaks shown in the magnified image to the right along the [010] direction crossed the allowed M-points at ½(501) and the R-points at ½(511). In addition, [100]-oriented streaks can also be seen on the left side of Figure 8a, as marked by dashed circles in multiple regions. These extra streaks across the superlattice points locations are also part of the diffuse scattering network.

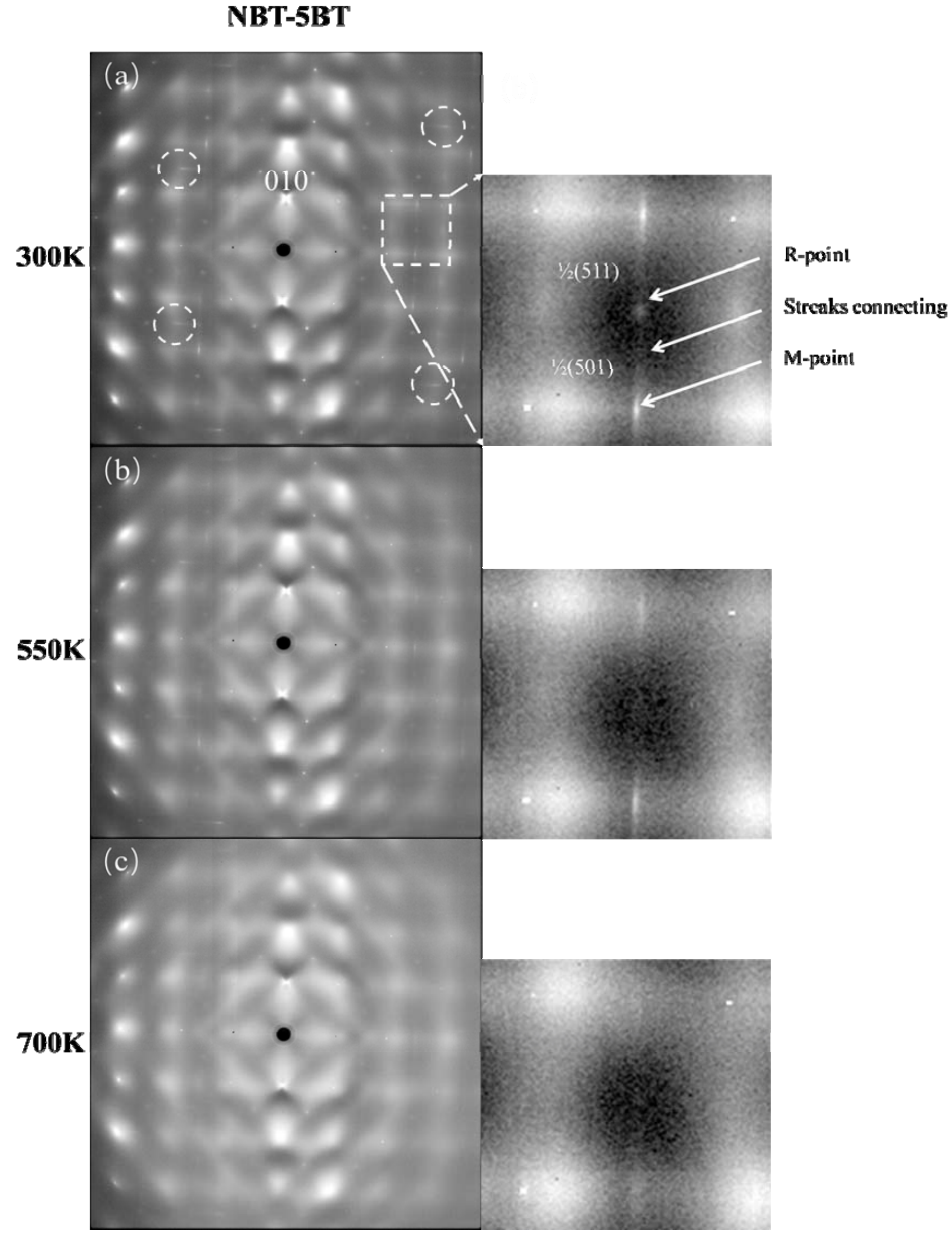

Figure 8: XRD scattering patterns tilted from the (HK0) planes for NBT-5BT at (a) 300K, (b) 550K and (c) 700K. The tilting angles were the same and were chosen by the maximum intensities of the R-points at ½(511) and ½(531). The smaller images on the right of each panel are higher resolution area images in order to better show the allowed M-points ½(501) and R-points ½(511). Extra [100]-oriented diffuse scattering streaks are marked by dashed circles in (a).

The temperature dependence of the diffuse scattering network was also investigated. Figures 8b-c show the same mesh scans as Figure 8a but at 550K and 700K. At 550K (Figure 8b), the intensity along [100]/[010] decreased, the M-point intensity slightly decreased, and the R-point was suppressed. When heating to 700K (Figure 8c), both the diffuse scattering streaks and the M-point intensities strongly decreased to the point of vanishing.

The remaining synchrotron XRD data are summarized in Figures 9a-b, which focus on two different R-points at ½(511) and ½(531) for various temperatures. The integration was accomplished in the same way as the M-point data process illustrated in Figure 3h-i. Furthermore, Figure 9c summarizes all the super-lattice reflection fitting results with temperature for the various M-points and R-points. All the peak fittings use Lorentzian functions. Red lines correspond to the same allowed M-points at ½(310) as shown in Figure 2 and Figure 3. Blue and black lines pertain to the same NBT-5BT crystal, but show results from two different R-points at ½(511) and ½(531). The peaks of ½(511) are too weak to be fit when temperature is higher than 400K and the same for ½(531) peak at 450K. The temperature difference of the intensity dropping between two R-points is caused by the curvature of the detector sampling surface in reciprocal space, causing unequal deviations from the precise R point locations. Thus, the later discussion will only focused on ½(531).

Figure 9c illustrates an important difference between the integrated intensities associated with the allowed M-points and the R-points. The M-points exhibit a nearly linear decrease in intensity with increasing temperature between 300K and 700K. Moreover, no anomalies were found at any critical temperature. In contrast, the R-points show a significant drop in intensity near the depolarization temperature T_d (403K). Thus, the data show that M-points and R-points coexist only in the ferroelectric phase region—but at higher temperatures, only M-points persist. Additionally, R-point ½(531) FWHMs of NBT-5BT have a mean value of 0.10042±0.02454 and a standard deviation of 0.01323. Thus, the R-point derived (R3c) PNR also has the same temperature-independent average size as M-point derived PNR.

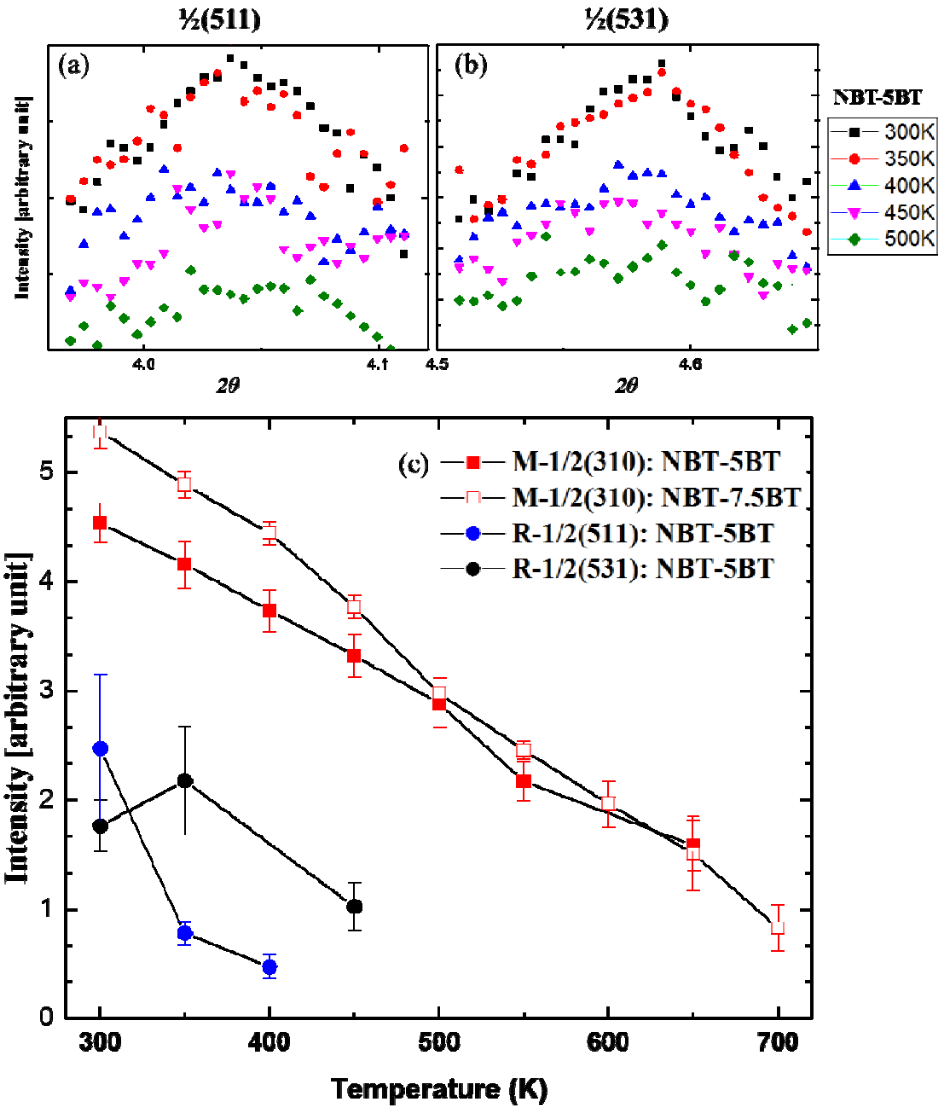

Figure 9: Top panel (a)(b): Integration of the NBT-5BT R-points intensity for (a) ½(511) and (b) ½(531) peaks with different temperatures. The integration process follows the Figure 3h-i. There are fixed offsets between the two neighboring curves to make comparison easier. Bottom panel (c): Temperature dependent super-lattice point intensity changes of NBT-5BT and NBT-7.5BT for the allowed M-point about ½(310) and R-point about ½(511)/ ½(531). The peaks were all fit by Lorentzian functions.

3.4. Inelastic neutron scattering in (HHL) plane

This section examines the inelastic component of the neutron intensities in the (HHL) plane. Near the Bragg peak, Figure 10 depicts transverse inelastic neutron scattering in the (002) zone. (Note that due to different propagation direction, the phonons are different from those discussed in Figure 4 and Figure 5.) Panels (a-g) illustrate the transverse phonon intensity and fitting results, with solid (open) dots indicating results from constant-Q (constant-E) cuts, respectively. It should be noted that the main part of fitting results, black and white dots, used the same fitting parameters of Figure 4, while the red dots represent findings from thinner constant-Q cuts (integrated from smaller Q-range, from 0.04 to 0.02), compared to the black ones, and the triangular dots indicate results of fits with larger uncertainty. Despite these minor differences, there are two common points for all the panels in this figure: (a) the TO phonon dispersions reach their maximum at E=16meV when q>0.2, and (b) the TA phonons were also nearly flat in E for q>0.15. Different from the Figure 5d-f, the M-point at the ½(110) is forbidden so there is no similar phonon connection here. Additionally, NBT-5BT and NBT-7.5BT have extra optical phonon signals near q=0 and E=13meV at 300K, which show softening at higher temperatures.

Similar to the bottom panel of Figure 4, the longitudinal phonons showed little response to changes in temperature or composition. Figure 10h only shows the phonons from NBT-5BT at 300K.

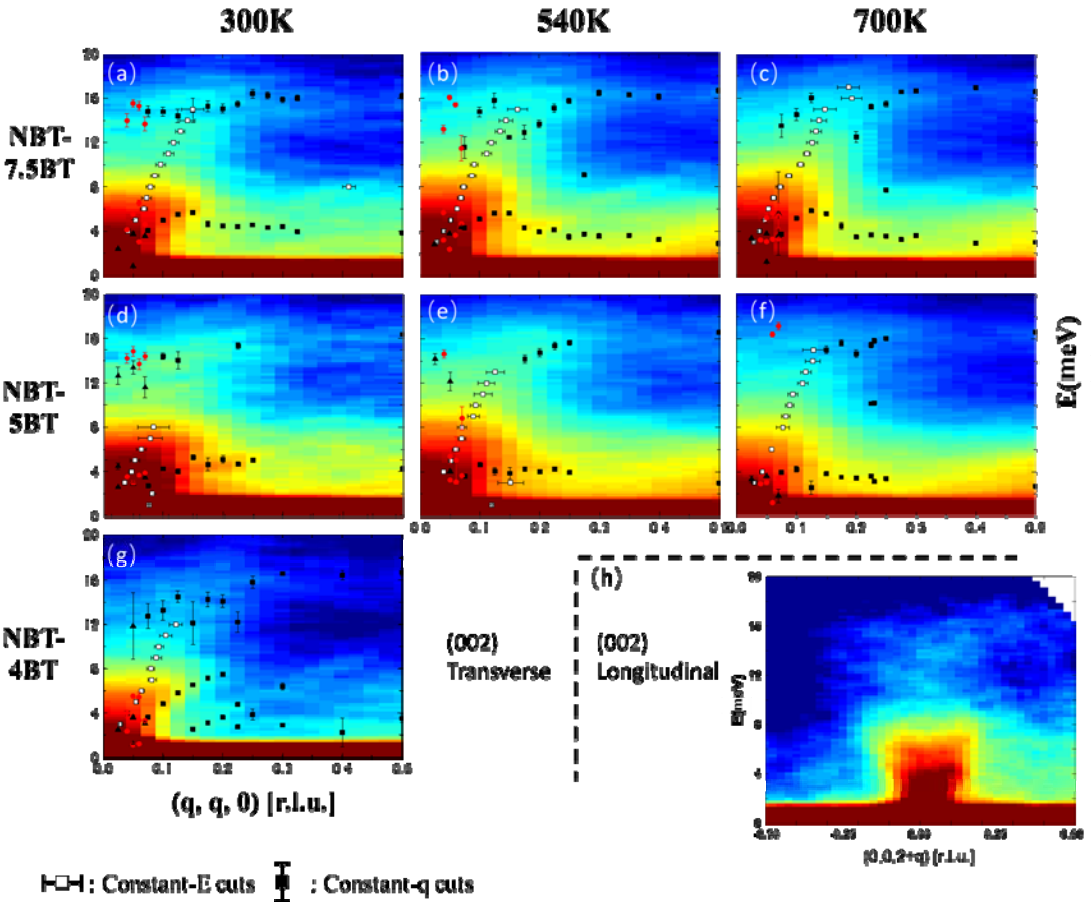

Figure 10: Inelastic neutron scattering taken near the (002) zone in the (HHL) plane. The main image is divided into three rows for transverse acoustic phonons (a)(b)(c) NBT-7.5BT, (d)(e)(f) NBT-5BT and (g) NBT-4BT, as well as three columns for (a)(d)(g) 300K, (b)(e) 540K and (c)(f) 700K. Longitudinal phonons are shown in (h) NBT-5BT at 300K. Solid dots indicating fitting results from constant-Q cuts, and open dots indicating those from constant-E cuts. The red dots represent fitting from thinner cuts in comparison to the black ones, and the triangular dots indicate fits with larger uncertainties.

Finally, we discuss phonons near the forbidden M-points. Figure 11 shows the INS intensity for transverse conditions near the M-point ½(-3, -3, 0) in the (HHL) plane. The dataset was folded along the [HH0] axis to improve statistics, so the R-point is located in the middle, while the M-point is situated on the right side.

Figure 11 also shows that, in addition to the elastic diffuse scattering streaks across the R-points and the M-points, a broad inelastic "band" could be observed between these super-lattice reflections. This signal could possibly correspond to damped fluctuations of soft tilt modes emerging from zone-boundary points. In contrast to the more clearly resolved acoustic phonons near the Bragg peaks (see Figure 10), these inelastic bands showed a strong dependence on composition, being most intense for x=5%. The energy width of this feature is about 6~8meV and changes little with temperature.

To confirm this feature, further slices (parallel to those in Figure 11 along [-H, H, 0]) were made. We find the thickness of this band of intensity to be less than 0.2r.l.u. along [HH0]. In addition, maps similar to those in Figure 6 but integrating only over finite energy transfer were made. Without the Al-ring interference in the higher energy range, the shape of this band in the (HHL) plane shows negligible changes with energy until the cuts reach the E>8meV. Similar to the results in Figure 5d-f, from compatibility relations between the M and R modes [30], the symmetry character of this inelastic band could be related to M_3-Δ_2-R_{25} modes, which is also notated as T_2 mode in work of Swainson et al. [37]. The inelastic bands also help to explain the shape of the M-point energy columns (see Figure 5) due to their same M_3 mode origin, as the intense scattering columns represent the perpendicular cuts of the bands at the M-points ends, and thus they have the same energy height (8meV).

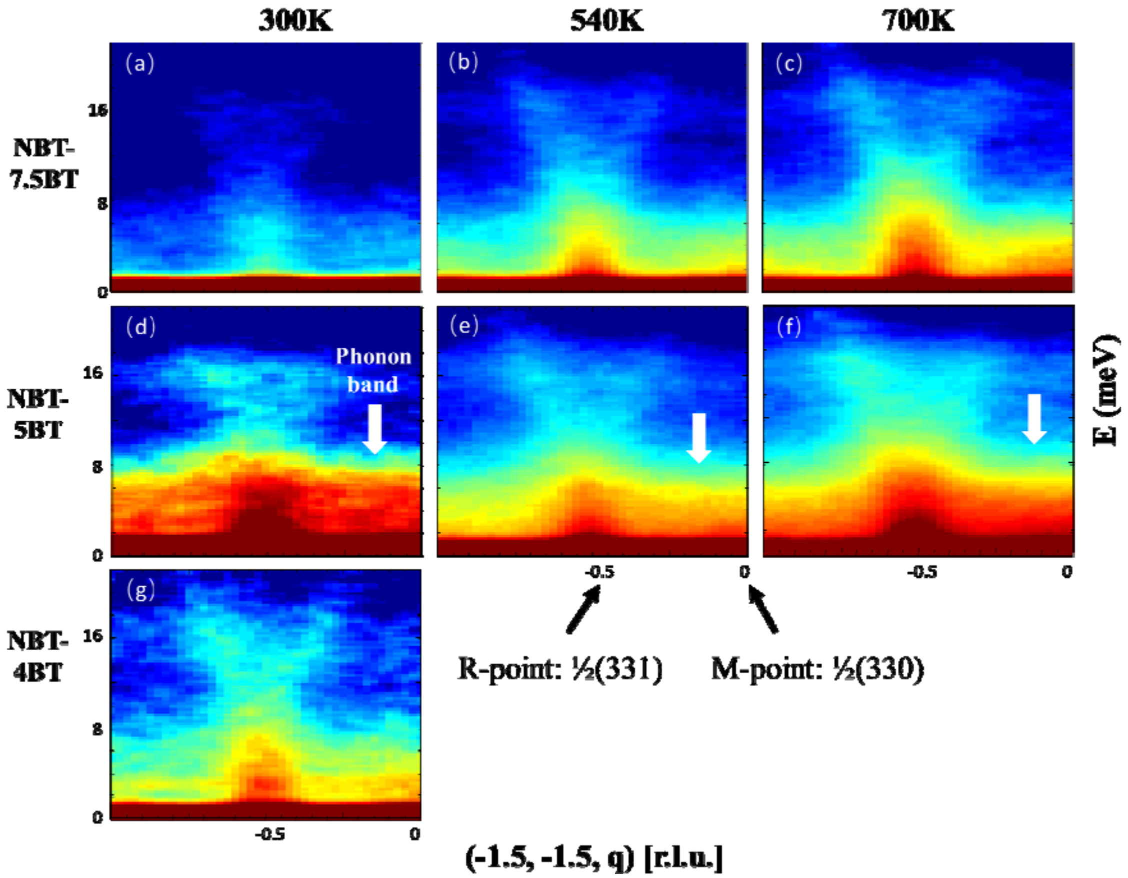

Figure 11: Inelastic neutron scattering taken near the forbidden M-point ½(-3, -3, 0) in the (HHL) plane. The figure is divided into three rows for compositions of (a)(b)(c) NBT-7.5BT, (d)(e)(f) NBT-5BT and (g) NBT-4BT; as well as three columns for temperatures of (a)(d)(g) 300K, (b)(e) 540K and (c)(f) 700K. All the images are plotted after being folded along [HH0] axis.

4. Discussion

4.1. Model of diffuse scattering network

Before the discussion on model of diffuse scattering network which links super-lattice points, a summary of observations in this work is list below:

Elastic:

1. Elastic diffuse scattering including oval-shaped and X-shaped diffuse scattering around different Bragg peaks are found in the (HK0) plane. Such a diffuse scattering pattern is characteristic of the tetragonal side of the MPB.
2. The ½(HH0) M-point is forbidden in both neutron and XRD elastic patterns, as previously reported [31]. However, our neutron results show weak and isotropic ½(-3,-3,0) reflections in the (HHL) plane, while diffuse ridges cross the forbidden ½(330) in the (HK0) plane. Additionally, these ridges become weak or absent towards the allowed M-point ½(510).
3. Diffuse streaks are found in the elastic scattering channel in the vicinity of the R-points that are oriented along [100]/[010] (see Figure 7). This feature is weakened significantly with increasing temperature near the dielectric constant maximum. These X-shaped features near the R-point super-lattice reflections are previously unreported, and differ from those around the Bragg peaks.

4. The diffraction intensity (see Figure 9) around the super-lattice reflections reveals that the R-points experiences an abrupt change near the ferroelectric phase transition at temperatures near T_d. In contrast, the intensity of the allowed M-points gradually decreases with increasing temperature between 300K and 700K. Also, our analysis of peaks at the M- and R-point shows nearly temperature-independent FWHM, which was not previously reported. Comparing the NBT-5BT and NBT-7.5BT, the integrated intensities at the M-points are stronger at room temperature for NBT-7.5BT, while the peaks for NBT-5BT were sharper.
5. Diffuse streaks in the elastic scattering are observed between the R-points and allowed M-points along [100]/[010] (see Figure 8). Such streaks have not been previously reported to our knowledge.

Inelastic:

1. A waterfall effect is seen in the INS near the (200) Bragg peak (see Figure 4). This waterfall feature has previously been reported in PMN and NBT relaxor-type solid solutions [26, 36, 38]. The waterfall feature is most pronounced near the MPB of NBT-5BT, which heretofore has not been reported.
2. Inelastic columns are observed near the allowed M-points only (see Figure 5), which are nearly temperature- and composition-independent over the ranges investigated for NBT-xBT. Similar broad columns have previously been reported for PMN by Swainson et al. [37], but were not been

reported for NBT-xBT solutions. Near the (210) zone, the Σ_3-M_3 connection suggests that these results from in-phase tilting modes.

3. A broad "band" of inelastic scattering, about 8 meV wide, connecting R-points and forbidden M-points (see Figure 11) is observed with INS. This band exhibited a strong intensity for the composition closest to the MPB. Note that the end of this band corresponds to the TA M_3 mode of the forbidden ½(330). We could not see similar intensity between the R-points and allowed M-point. This band and the inelastic columns (see Figure 5) appear to have the same origin, with the columns representing the perpendicular cuts of the phonon band across the M-points.

Figure 12 provides schematic summarizing observations. It incorporates both elastic (Figure 12a) and inelastic scattering (Figure 12b). In Figure 12a, the white spheres represent the pseudocubic Γ-points. The cyan sphere center is the R-point. The blue spheres represent the forbidden M-points shown in Figure 6, and comparing the allowed M-points in purple exhibited a spindle-shaped diffuse scattering (see Figure 2d). In addition to the super-lattice reflections, strong elastic diffuse streaks are identified between them, comprising a filamentary network along [100]/[010] directions (see Figures 7 and 8). The streaks network is illustrated in Figure 12a by the red rods that connect the R-points and allowed M-points. Several rotations of the elastic diffuse scattering schematic model of Figure 12a are provided in Figure 12c, which shows different 2-D and 3-D projections of the streaks network.

In Figure 12b, the phonons that cross the super-lattice points are summarized and their locations are marked by double arrow symbols. The Σ_3-M_3 connections (see Figure 5d-f) are illustrated in Figure 12b by red arrows. Also, the inelastic bands, M_3-Δ_2-R_{25} connections, between the forbidden M-points and R-points (see Figure 11) are shown as blue arrows in Figure 12b.

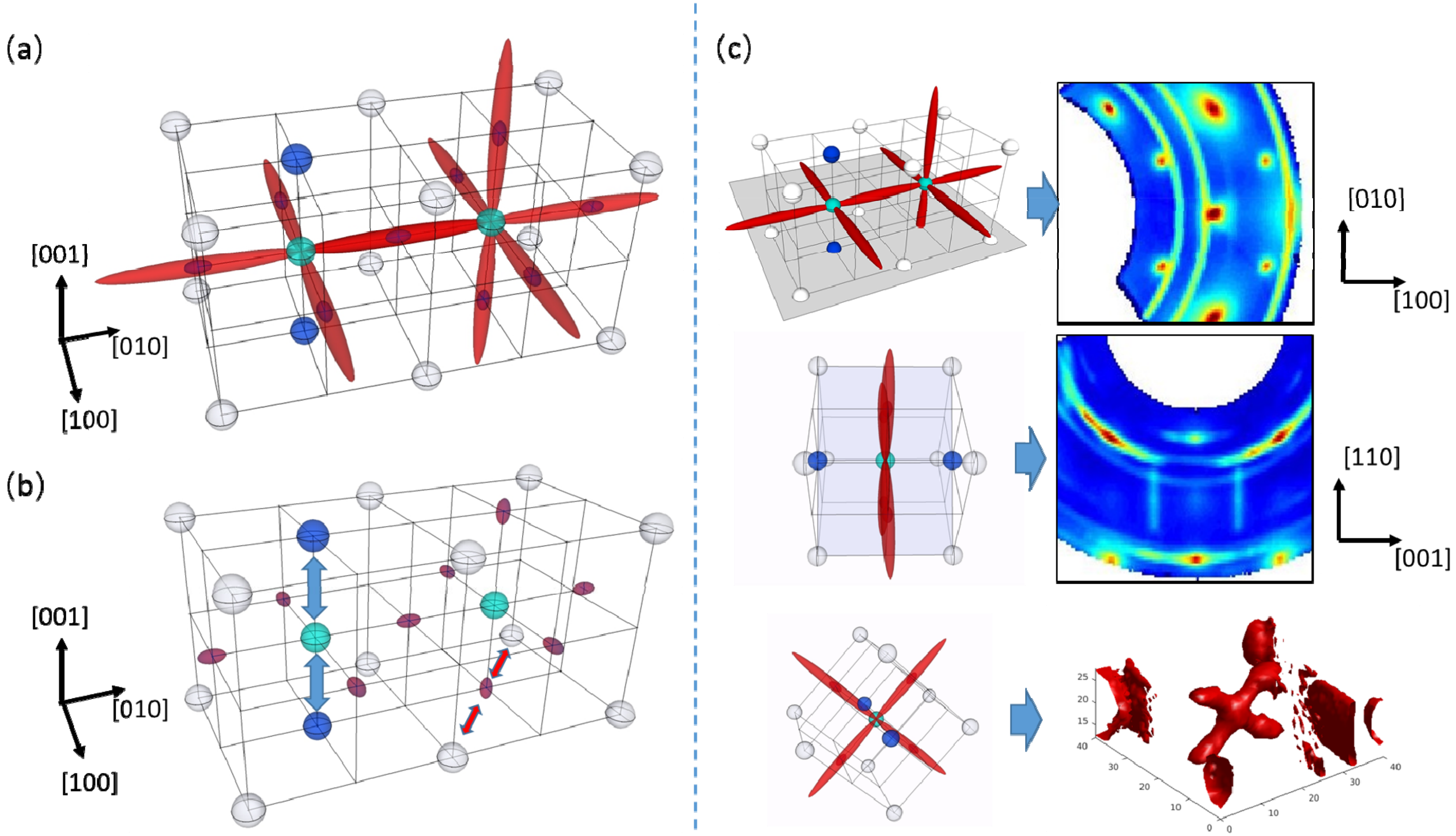

Figure 12: Schematic of diffuse scattering streaks for NBT-xBT: (a) Elastic network across the super-lattice points. (b) Inelastic phonon connections. (c) Demonstrations of how to offer the elastic slices from the schematic in (a). White spheres are Bragg peaks in the pseudocubic lattice, the R-point is marked by cyan spheres, the different types of M-points are marked by blue spheres and purple spindle-shape spheres.

4.2. Diffuse scattering

Diffuse scattering ridges about the (100) zone along the (110) are well established in both PMN-PT and NBT-BT, as also reported herein. Such diffuse scattering ridges are a common feature to both Pb-based and Pb-free perovskite relaxor solid solutions. These ridges have been attributed to nanoscale inhomogeneous polarization distributions along a given direction [23]. In real space, they reflect the presence of polar nanoregions (PNR) that organize into hierarchical domain structures along (110). Another common point is that this type of diffuse scattering is suppressed in the high-temperature range (>T_C) for both Pb-based and Pb-free relaxors, which illustrates a correlation to the presence of polarization. However, it should be noted that for PMN-PT [39], the (110)-oriented diffuse scattering is significant in PMN on the rhombohedral side of the MPB while the diffuse scattering from PNRs is very weak or absent on the tetragonal side of the MPB in favor of a long-range, structurally-ordered ground state.

NBT, on the rhombohedral side of the MPB, has been reported to exhibit "L" shape diffuse scattering patterns near (012) [23]; in contrast, NBT-5/7.5BT on the tetragonal side of the MPB features scattering patterns that are oval in shape and elongated in the <110> direction. Another study using neutron diffuse scattering by Ge et al. [4] investigated both A-site NBT and B-site PMN relaxors. comparing their similarities and differences in the geometry of the diffuse scattering patterns and the morphologies of the PNR distributions. The further diffuse scattering patterns of NBT and NBT-5.6BT showed A-site NBT-xBT has different PNR distribution, comparing to B-site PMN [4]. Specifically, prominent ridges in the elastic diffuse scattering intensity resulted in different types of contours. The ridges along the [100]/[010] directions cross at (hh0)/(-hh0) and generated "L" shaped patterns for NBT; conversely, the ridges along the [110] direction crossed at (h00)/(0k0) and generated the X-shaped patterns for NBT-5/7.5BT. These ridges disappeared gradually upon heating above the cubic-to-tetragonal phase transition temperature of T_{CT} =523°C [4]. Thus, these ridges across the Γ-points can be used to characterize different types of PNRs. In this work, typical diffuse scattering patterns of NBT-xBT near the MPB are observed.

NBT-xBT differs from PMN-xPT in another notable aspect, by featuring improper ferroelectric oxygen octahedral tilt systems. Yao et al. [22, 40] reported a hierarchical domain structure, where PNRs form on cooling within the geometrical restrictions imposed by the inheritance of a high temperatures ferroelastic phase consisting of nm-sized oxygen tilt domains. Dark field imaging in TEM of the super-lattice reflections revealed tilt domains of a few nm in size, which likely prevented a range of PNRs from achieving the elastic compatibility conditions of the relaxed state. Rather, a PNR distribution with a vortex morphology was recently shown to form [41]. Here, M-points and R-points in the diffraction patterns are better characterizations of the coexistence phases/PNRs comparing to the diffuse scattering patterns near the Γ-points [32]. The results of this study show that upon increasing temperature between 300K and 700K, the intensity of the allowed M-points gradually decreases, but the R-point intensity disappears near the ferroelectric phase transition (T_d). These findings lead to two conclusions: (a) the volume fraction of T-phase PNR changes linearly and is not significantly affected by the ferroelectric phase transition; (b) the changes of R-phase PNR is closely related to ferroelectric phase transition. Such PNR changing modes can successfully explain the origin of the frequency dispersion of temperature dependent of dielectric constant curves of NBT-xBT [42]. While near the T_d, there is T-phase/R-phase PNR coexistence, which causes the different frequency dispersion. While near the T_m, there is only T-phase PNR, so there is no dispersion at T_m. Further analysis reveals that the M-point and R-point peaks have nearly temperature-independent FWHM. Thus, it can be concluded that both T-phase and R-phase PNRs have nearly fixed average sizes. Comparing the NBT-5BT and NBT-7.5BT, it also can be concluded that stronger M-points for NBT-7.5BT means T-phase have more volume fractions herein, while the narrower FWHM for NBT-5BT signifies larger PNR average size as well as longer range of in-phase superlattice ordering.

As shown in the Figure 12, the super-lattice point linking diffuse scattering network shows a new feature of short-range ordering. The streak along [100]/[010] extends across the whole Brillouin zone between the R-points and the allowed M-points. This phenomenon not only reflects the M-point and R-point coexistence, which is already used to explain the electron diffraction (TEM) result [10, 32], but also indicates these different types of tilt domains are stacking together along the

[100]/[010] directions in short-range ordering. The long streaking along this direction may then demonstrate that the stacking sequence is not regular and that size of the tilt domains is not constant.

The net result of these competing processes is that the multiple domain ordering process (PNRs and tilt domains) may be prevented from reaching their elastically relaxed condition. If that is the case, then the polarization and different oxygen tilt systems would elastically constrain each other. Unlike in the PMN-xPT system, the PNR distribution would then not be as readily altered by applied field or stress (following adaptive phase theory), nor could the polarization of the monoclinic phase rotate as readily in an easy plane (following homogeneous theory). Rather, the primary mechanism for shape change would be a length extensional mode, as recently shown by Ge et al. [19]. As a consequence, the piezoelectric properties of NBT-xBT may be significantly lower than the analogous properties reported for Pb-based relaxor single crystal systems. To enhance the piezoelectricity in these Pb-free system, going forward, one should consider how to decouple the polarization from the oxygen tilt system.

Differing with the allowed M-points in (HK0) planes, weak and isotropic diffuse scattering patterns are found near the forbidden ½(330) M-points in (HHL) planes. These weak super-lattice reflections are due to the imperfections associated with the translational invariance of the tetragonal phase with average P4bm symmetry, and reflect the inherent inhomogeneity of the oxygen tilt and polarization subsystems. The stacking of the M-tilt and the R-tilt domains of nm-size, along with the presence of a high density of PNR boundaries, is far from the perfect symmetry for P4bm. Additionally, these forbidden M-points are not interconnected to either the R-points or allowed M-points via elastic diffuse scattering. However, this only considers the static distortions determine from elastic diffuse scattering. In fact, one also needs to consider the phonon dynamics of the inelastic diffuse scattering in order to fully understand how the different modes are interconnected.

4.3. Inelastic neutron scattering

It is found that the lattice dynamics of NBT-xBT are similar to those previously reported for PMN [37], except for a few important details. The first is the presence of the waterfall effect, and the second is the presence of inelastic intensity columns near the allowed M-points, which are very unusual given the fact that the line shape is localized in momentum, but broad in energy. No physical reason has yet been given to explain the existence of inelastic columns in PMN—and thus, by inference, with our report of their presence in NBT-xBT. Columns of inelastic intensity have been associated with a coupling of the lattice with other degrees of freedom [37]. Therefore, it is reasonable to attribute them in NBT-xBT to the coupling between polarization and oxygen tilt through rotostriction [43] over limited length scales in an inhomogeneous relaxor-like system. This speculation is supported by the fact that the presence of these inelastic columns is clearly temperature-independent over the temperature range that we investigated (300-700K). In prior research on PMN, the inelastic columns were found to soften with decreasing temperature below the dielectric maximum due to a softening of the optic phonon mode [37]. This behavior would suggest that the inelastic columns in NBT-xBT are not directly related to the formation of polarization, but rather persist into the high-temperature phase region where the M-type oxygen octahedral rotations remain present.

The close relationship between M-point columns and oxygen octahedral tilt systems is further confirmed from the presence of an acoustic mode connection that links allowed M-points to Γ-point (see Figure 5d-f). This Σ_3-M_3 connection, which is not reported in NBT [26], correlates the M-point columns with TA M_3 modes. This acoustic Σ_3-M_3 mode is stronger near the MPB and notably temperature-dependent. The M_3 mode is related to the oxygen octahedral in-phase tiltings and thus could explain the temperature independence of the M-point columns. Comparing to the case of NBT [26], the M_3 mode is more intense and localized at M-points in NBT-xBT near the MPB, presumably due to the enhanced M-point derived PNR with in-phase tiltings.

Another characteristic signature of the MPB region is the presence of inelastic bands connecting the R-points to the forbidden M-points in the (HHL) plane, as shown in Figure 11. This band of intensity is following the M_3-Δ_2-R_{25} phonon branches. Similar to the Σ_3-M_3 connections, due to its low energy and temperature-independence at the M-points, one can infer that this inelasitc band is the result of the coupling of the oxygen octahedral tilt modes. Indeed, this band-shaped M_3-Δ_2-R_{25}

mode is distinctly different compared to the previous Σ_3-M_3 mode as well as the soft optic modes at the M-point columns of PMN [37]. The enhanced intensity of this inelastic band at the MPB indicates the existence of the intermediate Δ_2 mode which helps coupling the M_3 and R_{25} tilting modes. The Δ_2 mode is also a tilting mode but related to the tilting along the [HH0] axis. Similar to the bridging monoclinic phase in PZN-xPT at the MPB [44], such a mode could also lower the energy barrier between the M_3 and R_{25} tilting modes.

Thus, in addition to the importance of phase coexistence, a better understanding of dynamical features represents a key avenue for developing next-generation piezoelectric materials for potential applications. In other word, phase coexistence alone, which is a characteristic of many Pb-based and Pb-free compositions even away from MPB, cannot ensure high piezoelectric properties in Pb-free systems. Specific dynamical features, such as the inelastic bands or M_3-Δ_2-R_{25} mode are also required, to relax the constraints of the mixed oxygen tilt state. By redistributing energy between the different modes, the system can partially relax, and the oxygen tilt domains and PNRs can readjust and better accommodate each other. This process, in turn, can allow the material to express higher induced shape changes in response to stimuli in comparison to a response facilitated by a length extensional mechanism.

5. Conclusion

We systematically studied the NBT-xBT single crystals with neutron and x-ray scattering, for several temperatures and compositions across the MPB. Typical oval-shape [110] direction diffuse scattering patterns were observed near the Γ-points (210), indicating the MPB compositions. In addition, a super-lattice point linking diffuse scattering network was observed, revealing a ferroelectric and short-range ordering PNR static stacking morphology. The evolution of super-lattice points with temperature also showed that the size of related PNRs changes weakly with temperature. The lattice dynamics measurements focused on both phonon dispersions near the Γ-points and super-lattice points. A waterfall feature was observed in the TO mode near the (200) and was most enhanced in NBT-5BT at room temperature. For super-lattice points, two types of dynamical signatures are found. One between the M-points and Γ-points along the [110] direction, consistent with M-related tilting modes. The other between the M-points and R-points along the [001] direction indicating the existence of an intermediate tilting mode, which could be essential in the high performance of those compositions near the MPB.

6. Acknowledgments

Authors C.L. and D.V. would like to thank the ONRL-GO program for support of this work through the Laboratory Directed Research and Development Program of Oak Ridge National Laboratory, managed by UT-Battelle, LLC, for the U.S. DOE, and J.F.L. would like to thank the Office of Naval Research for the support of this work (N00014-13-1-0049). O.D. and D.B. acknowledge funding from the U.S. Department of Energy, Office of Science, Basic Energy Sciences, Materials Sciences and Engineering Division, under the Early Career Award No. DE-SC0016166. Authors X.L. and H.L. acknowledge the Natural Science Foundation of China under Grant No. 51332009, and the Shanghai Rising-Star Program No. 11QA1407500. The use of Oak Ridge National Laboratory's Spallation Neutron Source was sponsored by the Scientific User Facilities Division, Office of Basic Energy Sciences, US Department of Energy. This research used resources of the Advanced Photon Source, a U.S. Department of Energy (DOE) Office of Science User Facility operated for the DOE Office of Science by Argonne National Laboratory under Contract No. DE-AC02-06CH11357.

7. Reference

1. Cochran, W., *Dynamical, Scattering and Dielectric Properties of Ferroelectric Crystals.* Advances in Physics, 1969. **18**(72): p. 157-&.
2. Foster, C.M., Z. Li, M. Grimsditch, S. Chan, and D.J. Lam, *Anharmonicity of the lowest-frequency A1(TO) phonon in PbTiO3.* Phys Rev B Condens Matter, 1993. **48**(14): p. 10160-10167.
3. Tomeno, I., J.A. Fernandez-Baca, K.J. Marty, K. Oka, and Y. Tsunoda, *Simultaneous softening of acoustic and optical modes in cubic PbTiO${}_{3}$.* Physical Review B, 2012. **86**(13): p. 134306.
4. Ge, W., C.P. Devreugd, D. Phelan, Q. Zhang, M. Ahart, J. Li, H. Luo, L.A. Boatner, D. Viehland, and P.M. Gehring, *Lead-free and lead-basedABO3perovskite relaxors with mixed-valenceA-site andB-site disorder: Comparative neutron scattering structural study of (Na1/2Bi1/2)TiO3and Pb(Mg1/3Nb2/3)O3.* Physical Review B, 2013. **88**(17): p. 174115.
5. Hirota, K., Z.G. Ye, S. Wakimoto, P.M. Gehring, and G. Shirane, *Neutron diffuse scattering from polar nanoregions in the relaxor Pb(Mg1/3Nb2/3)O-3.* Physical Review B, 2002. **65**(10): p. 104105.
6. Stock, C., G.Y. Xu, P.M. Gehring, H. Luo, X. Zhao, H. Cao, J.F. Li, D. Viehland, and G. Shirane, *Neutron and x-ray diffraction study of cubic [111] field-cooled Pb(Mg1/3Nb2/3)O-3.* Physical Review B, 2007. **76**(6): p. -.
7. Xu, G.Y., *Probing local polar structures in PZN-xPT and PMN-xPT relaxor ferroelectrics with neutron and x-ray scattering.* International Conference on Frustration in Condensed Matter (Icfcm), 2011. **320**: p. 012081.
8. Leontsev, S.O. and R.E. Eitel, *Progress in engineering high strain lead-free piezoelectric ceramics.* Sci Technol Adv Mater, 2010. **11**(4): p. 044302.
9. Takenaka, T. and H. Nagata, *Current status and prospects of lead-free piezoelectric ceramics.* Journal of the European Ceramic Society, 2005. **25**(12): p. 2693-2700.
10. Ma, C., H. Guo, S.P. Beckman, and X. Tan, *Creation and Destruction of Morphotropic Phase Boundaries through Electrical Poling: A Case Study of Lead-Free (Bi_{1/2}Na_{1/2})TiO_{3}-BaTiO_{3} Piezoelectrics.* Physical Review Letters, 2012. **109**(10): p. 107602.
11. Glazer, A.M., *The classification of tilted octahedra in perovskites.* Acta Crystallographica Section B Structural Crystallography and Crystal Chemistry, 1972. **28**(11): p. 3384-3392.
12. Setyawan, W. and S. Curtarolo, *High-throughput electronic band structure calculations: Challenges and tools.* Computational Materials Science, 2010. **49**(2): p. 299-312.
13. Acosta, M., L.A. Schmitt, C. Cazorla, A. Studer, A. Zintler, J. Glaum, H.J. Kleebe, W. Donner, M. Hoffman, J. Rodel, and M. Hinterstein, *Piezoelectricity and rotostriction through polar and non-polar coupled instabilities in bismuth-based piezoceramics.* Scientific Reports, 2016. **6**: p. 8.
14. Yao, J.J., N. Monsegue, M. Murayama, W.N. Leng, W.T. Reynolds, Q.H. Zhang, H.S. Luo, J.F. Li, W.W. Ge, and D. Viehland, *Role of coexisting tetragonal regions in the rhombohedral phase of Na0.5Bi0.5TiO3-xat.%BaTiO3 crystals on enhanced piezoelectric*

properties on approaching the morphotropic phase boundary. Applied Physics Letters, 2012. **100**(1): p. 012901.

15. Park, S.E. and T.R. Shrout, *Ultrahigh strain and piezoelectric behavior in relaxor based ferroelectric single crystals.* Journal of Applied Physics, 1997. **82**(4): p. 1804-1811.
16. Cross, L.E., *Relaxorferroelectrics: An overview.* Ferroelectrics, 1994. **151**(1): p. 305-320.
17. Guo, Y.P., H.S. Luo, D. Ling, H.Q. Xu, T.H. He, and Z.W. Yin, *The phase transition sequence and the location of the morphotropic phase boundary region in (1-x)[Pb(Mg1/3Nb2/3)O-3]-xPbTiO(3) single crystal.* Journal of Physics-Condensed Matter, 2003. **15**(2): p. L77-L82.
18. Viehland, D.D. and E.K.H. Salje, *Domain boundary-dominated systems: adaptive structures and functional twin boundaries.* Advances in Physics, 2014. **63**(4): p. 267-326.
19. Ge, W., C. Luo, Q. Zhang, C.P. Devreugd, Y. Ren, J. Li, H. Luo, and D. Viehland, *Ultrahigh electromechanical response in (1−x)(Na0.5Bi0.5)TiO3-xBaTiO3 single-crystals via polarization extension.* Journal of Applied Physics, 2012. **111**(9): p. 093508.
20. Zhang, Q.H., X.Y. Zhao, R.B. Sun, and H.S. Luo, *Crystal growth and electric properties of lead-free NBT-BT at compositions near the morphotropic phase boundary.* Physica Status Solidi a-Applications and Materials Science, 2011. **208**(5): p. 1012-1020.
21. Soukhojak, A.N., H. Wang, G.W. Farrey, and Y.M. Chiang, *Superlattice in single crystal barium-doped sodium bismuth titanate.* Journal of Physics and Chemistry of Solids, 2000. **61**(2): p. 301-304.
22. Yao, J., L. Yan, W. Ge, L. Luo, J. Li, D. Viehland, Q. Zhang, and H. Luo, *Evolution of domain structures in Na1/2Bi1/2TiO3single crystals with BaTiO3.* Physical Review B, 2011. **83**(5): p. 054107.
23. Zhang, H.W., G.C. Deng, A.J. Studer, X.B. Li, X.Y. Zhao, and H.S. Luo, *Neutron diffuse scattering of (1-x)(Na0.5Bi0.5)TiO3-xBaTiO(3) relaxor ferroelectric single crystals.* Scripta Materialia, 2014. **86**: p. 5-8.
24. Gehring, P.M., *Neutron Diffuse Scattering in Lead-Based Relaxor Ferroelectrics and Its Relationship to the Ultra-High Piezoelectricity.* Journal of Advanced Dielectrics, 2012. **02**(02): p. 1241005.
25. Xu, G.Y., G. Shirane, J.R.D. Copley, and P.M. Gehring, *Neutron elastic diffuse scattering study of Pb(Mg1/3Nb2/3)O-3.* Physical Review B, 2004. **69**(6): p. 064112.
26. Deng, G.C., S. Danilkin, H.W. Zhang, P. Imperia, X.B. Li, X.Y. Zhao, and H.S. Luo, *Dynamical mechanism of phase transitions in A-site ferroelectric relaxor (Na1/2Bi1/2) TiO3.* Physical Review B, 2014. **90**(13).
27. Vakhrushev, S.B., B.E. Kvyatkovskii, N.M. Okuneva, E.L. Plachenova, and P.P. Syrnikov, *Phase-Transitions in Sodium Bismuth Titanate.* Jetp Letters, 1982. **35**(3): p. 134-137.
28. Shapiro, S.M., I.A. Zaliznyak, L. Passell, V.J. Ghosh, W.J. Leonhardt, and M.E. Hagen, *HYSPEC: A crystal time-of-flight hybrid spectrometer for the spallation neutron source with polarization capabilities.* Physica B-Condensed Matter, 2006. **385-86**: p. 1107-1109.
29. Winn, B., U. Filges, V.O. Garlea, M. Graves-Brook, M. Hagen, C.Y. Jiang, M. Kenzelmann, L. Passell, S.M. Shapiro, X. Tong, and I. Zaliznyak, *Recent progress on HYSPEC, and its polarization analysis capabilities.* Qens/Wins 2014 - 11th International Conference on Quasielastic Neutron Scattering and 6th International Workshop on Inelastic Neutron Spectrometers, 2015. **83**.
30. Cowley, R.A., *Lattice Dynamics + Phase Transitions of Strontium Titanate.* Physical Review, 1964. **134**(4a): p. A981-+.
31. Ge, W.W., C.T. Luo, C.P. Devreugd, Q.H. Zhang, Y. Ren, J.F. Li, H.S. Luo, and D. Viehland, *Direct evidence of correlations between relaxor behavior and polar nano-regions in*

relaxor ferroelectrics: A case study of lead-free piezoelectrics Na0.5Bi0.5TiO3-x%BaTiO3. Applied Physics Letters, 2013. **103**(24): p. 241914.

32. Yao, J.J., N. Monsegue, M. Murayama, W.N. Leng, W.T. Reynolds, Q.H. Zhang, H.S. Luo, J.F. Li, W.W. Ge, and D. Viehland, *Role of coexisting tetragonal regions in the rhombohedral phase of Na0.5Bi0.5TiO3-xat.%BaTiO3 crystals on enhanced piezoelectric properties on approaching the morphotropic phase boundary.* Applied Physics Letters, 2012. **100**(1).
33. Laijun, L., K. Michael, S. Ljubomira Ana, E. Helmut, F. Liang, F. Hartmut, H. Markus, and H. Manuel, *Structure and dielectric dispersion in cubic-like 0.5K 0.5 Na 0.5 NbO 3 -0.5Na 1/2 Bi 1/2 TiO 3 ceramic.* EPL (Europhysics Letters), 2016. **114**(4): p. 47011.
34. Kitanaka, Y., M. Ogino, K. Hirano, Y. Noguchi, M. Miyayama, Y. Kagawa, C. Moriyoshi, Y. Kuroiwa, S. Torii, and T. Kamiyama, *Crystal Structural Analyses of Ferrielectric Tetragonal (Bi1/2Na1/2)TiO3-7%BaTiO3 Powders and Single Crystals.* Japanese Journal of Applied Physics, 2013. **52**(9).
35. . ©2015 by Fachinformationszentrum Karlsruhe, ICSD code: 189275: https://www.fiz-karlsruhe.de/icsd.html.
36. Gehring, P.M., S. Wakimoto, Z.G. Ye, and G. Shirane, *Soft mode dynamics above and below the Burns temperature in the relaxor Pb(Mg1/3Nb2/3)O3.* Phys Rev Lett, 2001. **87**(27 Pt 1): p. 277601.
37. Swainson, I.P., C. Stock, P.M. Gehring, G.Y. Xu, K. Hirota, Y. Qiu, H. Luo, X. Zhao, J.F. Li, and D. Viehland, *Soft phonon columns on the edge of the Brillouin zone in the relaxor PbMg1/3Nb2/3O3.* Physical Review B, 2009. **79**(22): p. -.
38. Ondrejkovic, P., J. Hlinka, M. Kempa, J. Kulda, H. Luo, and Q. Zhang, *Inelastic neutron scattering study of lead-free relaxor ferroelectric (Na0.5Bi0.5)0.96Ba0.04TiO3single crystal.* Phase Transitions, 2011. **84**(9-10): p. 829-836.
39. Stock, C., D. Ellis, I.P. Swainson, G.Y. Xu, H. Hiraka, Z. Zhong, H. Luo, X. Zhao, D. Viehland, R.J. Birgeneau, and G. Shirane, *Damped soft phonons and diffuse scattering in 40%Pb(Mg1/3Nb2/3)O-3-60%PbTiO3.* Physical Review B, 2006. **73**(6): p. -.
40. Yao, J.J., Y.D. Yang, N. Monsegue, Y.X. Li, J.F. Li, Q.H. Zhang, W.W. Ge, H.S. Luo, and D. Viehland, *Effect of Mn substituents on the domain and local structures of Na1/2Bi1/2TiO3-BaTiO3 single crystals near a morphotropic phase boundary.* Applied Physics Letters, 2011. **98**(13).
41. Luo, C.T., Y.J. Wang, W.W. Ge, J.F. Li, D. Viehland, O. Delaire, X.B. Li, and H.S. Luo, *Hierarchical domain structure of lead-free piezoelectric (Na-1/2 Bi-1/2)TiO3-(K-1/2 Bi-1/2)TiO3 single crystals.* Journal of Applied Physics, 2016. **119**(17).
42. Ge, W.W., C.T. Luo, Q.H. Zhang, Y. Ren, J.F. Li, H.S. Luo, and D. Viehland, *Evolution of structure in Na0.5Bi0.5TiO3 single crystals with BaTiO3.* Applied Physics Letters, 2014. **105**(16): p. 162913.
43. Acosta, M., L.A. Schmitt, C. Cazorla, A. Studer, A. Zintler, J. Glaum, H.J. Kleebe, W. Donner, M. Hoffman, J. Rodel, and M. Hinterstein, *Piezoelectricity and rotostriction through polar and non-polar coupled instabilities in bismuth-based piezoceramics.* Sci Rep, 2016. **6**: p. 28742.
44. Fu, H. and R.E. Cohen, *Polarization rotation mechanism for ultrahigh electromechanical response in single-crystal piezoelectrics.* Nature, 2000. **403**(6767): p. 281-3.